

Ultrafast carrier dynamics in epitaxial graphene nanoribbons studied by time-resolved terahertz spectroscopy

Arvind Singh¹, Hynek Němec¹, Jan Kunc², and Petr Kužel^{1}*

¹ *FZU - Institute of Physics of the Czech Academy of Sciences, Na Slovance 2
18221 Prague 8, Czech Republic*

² *Faculty of Mathematics and Physics, Charles University, Ke Karlovu 3,
12116 Prague 2, Czech Republic*

* kuzelp@fzu.cz

Abstract: Optical pump-terahertz probe spectroscopy has been used to investigate ultrafast photo-induced charge carrier transport in epitaxial graphene nanoribbons. The picosecond THz photoconductivity first increases with an increasing pump fluence and then it saturates at high fluences. This behavior is due to an interplay between contributions of the directly photoexcited carriers and the secondary carriers, which are equilibrium conduction band carriers strongly heated by the carrier-carrier scattering process after the photoexcitation. This phenomenon leads to a non-monotonic variation of the carrier mobility and plasmonic resonance frequency as a function of the pump fluence and, at higher fluences, to a balance between a decreasing carrier scattering time and an increasing Drude weight. In addition, a weak carrier localization occurring at low pump fluences is progressively lifted as a result of increasing initial carrier temperature.

Keywords: epitaxial graphene, ultrafast photoconductivity, ultrafast carrier dynamics, terahertz

1. Introduction

Hot carriers in graphene exhibit fascinating physical properties that are distinctly different from the response of conventional semiconductors or metals. [1–5] This distinction arises predominantly due to the remarkably low electronic heat capacity of massless Dirac fermions, characterized by a linear electronic dispersion with strong carrier-carrier interactions and relatively weak coupling between the electronic and phononic systems. [6–11] Notably, photo-carriers can be easily excited at energies well above the Fermi level, emphasizing the subsequent carrier relaxation mechanisms pivotal for the functionality of opto-electronic

devices. In addition, graphene exhibits the strongest nonlinear THz response to date, which is attributed to hot carrier dynamics, [12–15] enabling, e.g., efficient high harmonic generation and paving the way for practical graphene-based applications in ultrafast (opto-)electronics operating at THz frequencies.

Understanding the transport of photo-induced charge carriers on ultrafast timescale in graphene-based nanostructures is essential for their further potential applications, especially in high-power electronics and optoelectronics. Optical pump-terahertz probe spectroscopy has proven to be a powerful non-contact technique for investigating these phenomena with sub-picosecond time resolution. [10] In this study, we apply this spectroscopic tool to study the charge carrier transport properties on picosecond timescale in epitaxial graphene nanoribbons as a function of the excitation fluence. Specifically, we focus on elucidating the non-linear scaling behavior of the ultrafast THz photoconductivity with the optical pump fluence, and its implications for the behavior of the carrier mobility, nanoscale carrier confinement and plasmonic response.

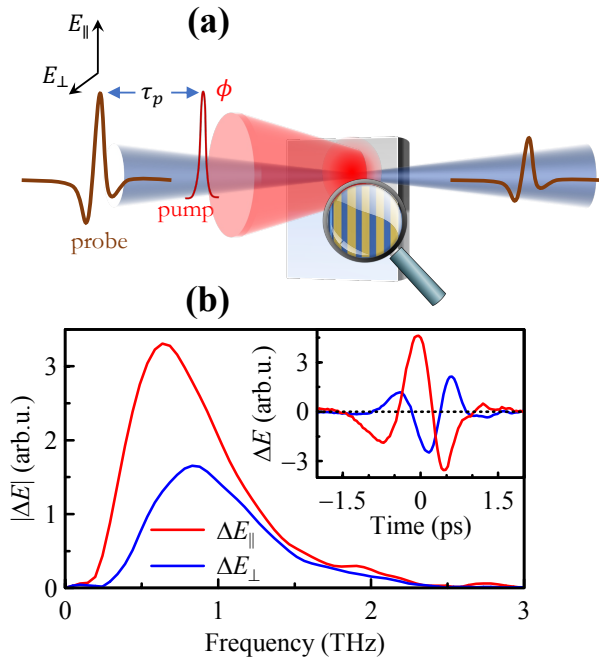


Figure 1: (a) Experimental schematic for optical pump – THz probe spectroscopy. Measurements are performed with THz electric field polarization both parallel and perpendicular to the graphene nanoribbons in a collinear geometry. (b) Examples of differential signals from graphene ribbons measured at 2 ps after photoexcitation for both THz polarizations: time domain waveforms in the inset and frequency domain amplitudes in the main plot.

2. Experimental part

The graphene nanoribbons studied here are prepared in three steps. Initially, a graphene layer is epitaxially grown on 6H-SiC substrate by thermal decomposition technique; [16]

subsequently, hydrogen intercalation is performed to decouple the graphene layer from the substrate (so called quasi-free standing single layer graphene is formed). [17] Finally, a large area nanoribbon array is fabricated using an electron beam lithography technique with a graphene ribbon width $w = 3400$ nm and a gap between the ribbons $g = 500$ nm (i.e., a period of the array $L = 3900$ nm). [18]

Figure 1(a) shows the experimental scheme which is used to measure the transient transmission of the epitaxial graphene nanoribbon sample. The optical pulses (time duration of 40 fs, wavelength of 800 nm and a repetition rate of 5 kHz) are delivered from a Ti:sapphire amplifier (Spitfire ACE, Spectra Physics). They are used for the sample photoexcitation at 800 nm and also for THz emission and detection ensured by a pair of (110) oriented 1 mm thick ZnTe crystals. The optical pump and terahertz probe pulse are collinearly incident on the sample surface covered by a 4 mm aperture. The pump beam is expanded in space to a spot with FWHM exceeding 7 mm to excite the sample homogeneously within the aperture.

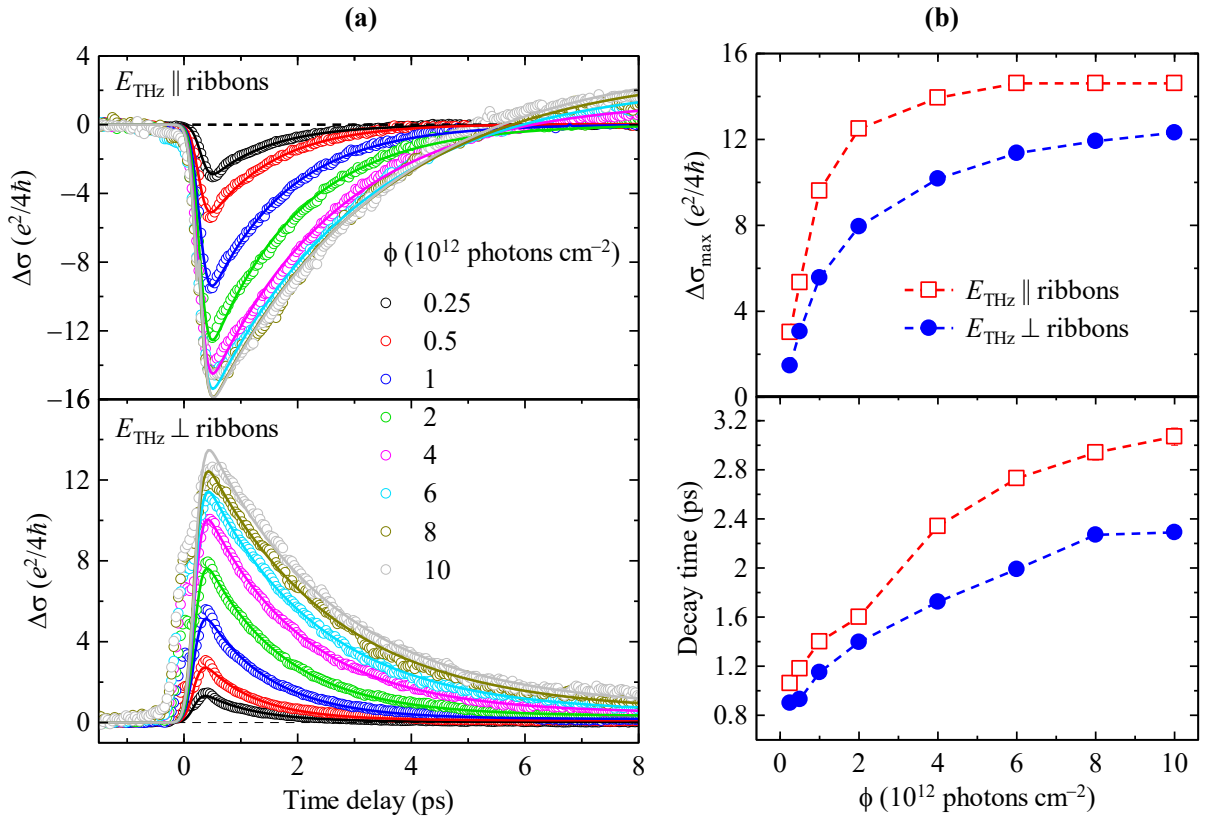


Figure 2: (a) Time-resolved THz photoconductivity (spectrally averaged) of graphene ribbons for several absorbed pump fluences in parallel (top) and perpendicular (bottom) configurations of probing THz electric field. Solid lines in the kinetic signal are fits using a mono-exponential decaying function convolved with the Gaussian probe pulse, Eq. (2). (b) Parameters extracted from the fit. Top: Photoconductivity amplitude; bottom: decay time as a function of the excitation fluence.

3. Results and discussion

Figure 2(a) shows the picosecond dynamics of the average transient THz photoconductivity for both polarizations of the probing THz field with respect to the graphene ribbons. The curves (so called pump-probe scans) are measured at the absolute maximum of the differential waveform ΔE as a function of the pump-probe delay. The differential transmission ΔE is directly related to the (spectrally averaged) photoconductivity; in the thin film approximation and small signal limit ($\Delta E \ll E_0$) we obtain [19]

$$\Delta\sigma = -\frac{1 + N_s}{z_0} \frac{\Delta E}{E_0} \quad (1)$$

where E_0 is a reference signal (transmitted THz field with the pump beam off), N_s (≈ 3.13) is the THz refractive index of the SiC substrate and z_0 is the vacuum wave impedance. The small signal limit is well satisfied in our experiments since $\Delta E/E_0 < 10\%$ even for the highest pump fluence used. A nonlinear scaling of the dynamics versus the pump photon fluence absorbed in the graphene layer can be clearly observed in Fig. 2. Note also the different signs of the two curves (for the parallel and perpendicular configuration), which have been discussed in [18] and which will be briefly revisited later in this paper in relation with the measured time-resolved THz spectra. The temporal evolution of the pump-induced THz transient dynamics is analyzed simply by a numerical fit of the experimental data using the following response function:

$$\Delta\sigma = \Delta\sigma_{\text{SiC}} + \left[H(t - t_0) \times \Delta\sigma_{\text{max}} \exp\left(\frac{t_0 - t}{\tau_c}\right) \right] \otimes G(t) \quad (2)$$

where, $H(t)$ is the Heaviside function and $G(t)$ is an instrumental Gaussian time profile; the symbol \otimes represents the convolution operation. The parameter $\Delta\sigma_{\text{SiC}}$ accounts for the substrate contribution, while $\Delta\sigma_{\text{max}}$ and τ_c characterize the amplitude and decay time of the transient response of the graphene film, respectively.

Figure 2(b) presents the fitting outcomes: amplitude of the response, $\Delta\sigma_{\text{max}}$ (corresponding to the peak graphene conductivity in time), and the decay time, τ_c , as a function of absorbed pump photon fluence. The photoconductivity amplitude first scales linearly with the excitation power and it saturates for high excitation fluences for both configurations. The lifetime progressively increases with increasing excitation fluence.

These observations can be explained as follows. Upon photoexcitation, primary electron-hole pairs are generated, initiating a sequence of carrier-carrier scattering events. This process involves the transfer of energy deposited by the pump beam and initially acquired by the excess

carriers towards the conduction carriers close to the Fermi level, which are then promoted to higher energies, thus creating a distribution of secondary hot carriers.[1] At lower fluences the concentration of excess carriers is low and the transient THz signal is essentially due to an increase in the effective temperature of the carrier distribution. As the absorbed photon density increases, the observed increase in the photoconductivity signal can be attributed to a higher temperature of the hot carrier distribution. Here, the change in the photoconductivity is directly linked to secondary hot-carrier excitation processes. Since the density of secondary hot carriers is limited by the doping level, further increase in the pump fluence inevitably leads to the photoconductivity saturation. It is worth noting that, regardless of the sign of the photoconductivity for the two THz probing polarizations observed in Fig. 2(a), the fluence dependence of the extracted parameters follows a similar trend (with a minor renormalization caused by the spectral shift of the plasmonic response in the perpendicular configuration), thereby validating the explanation discussed above for both cases.

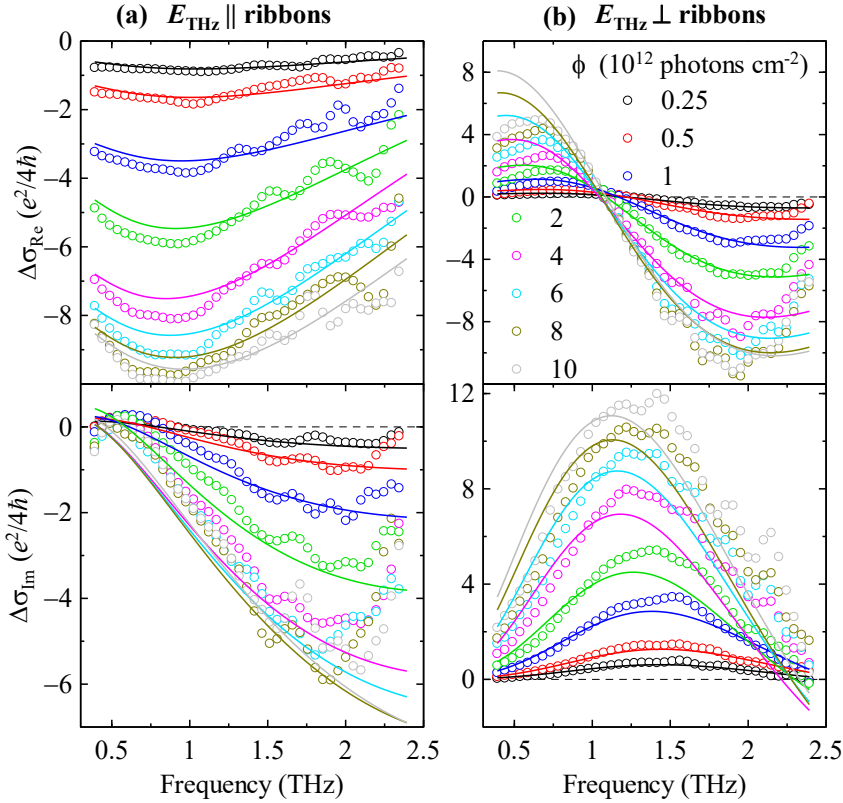


Figure 3: Transient sheet conductivity spectra as a function of the absorbed pump fluence for the pump-probe delay of 2 ps after photoexcitation in parallel (a) and perpendicular (b) configurations. Symbols: experimental points, lines: with the model defined by Eqs. (3)–(8).

For a more quantitative analysis of the photo-induced THz response of graphene nanoribbons, we measured transient THz waveforms 2 ps after photoexcitation for the same

set of the absorbed pump fluences and we calculated the photoconductivity spectra using Eq. (1), see Fig. 3. For the parallel configuration, the real part of the photoconductivity is negative over the whole accessible frequency range; this is due to the intraband conductivity reduction due to the heating of excess carriers and it correlates with the enhanced transparency signal observed in Fig. 2(a), top panel. For the perpendicular configuration, one observes a zero crossing in $\Delta\sigma_{\text{Re}}$, which is caused by a spectral shift of the plasmonic response upon photoexcitation. On the first glance, this observation might look inconsistent with the positive contribution to the spectral average observed in Fig. 2(a), bottom panel. However, note that the THz probing pulses exhibit the maximum power roughly in the spectral interval of 0.7–1 THz, see Fig. 1(b), i.e., the sample response in this particular range determines the global aspect of the transient time-domain waveforms, which then present a dominating negative half-cycle [blue curve in the inset of Fig. 1(b)] corresponding to a positive average photoconductivity in agreement with Eq. (1).

The ultrafast photoconductivity spectra are fitted using the following model:

$$\Delta\sigma(\omega, \phi) = \sigma_{\perp,\parallel}^e(\omega, \phi) - \sigma_{\perp,\parallel}(\omega) + \sigma_{\text{SiC}}(\omega, \phi), \quad (3)$$

which involves the graphene sheet photoconductivity (the difference between the sheet conductivity of the excited state $\sigma_{\perp,\parallel}^e$ and of the ground state $\sigma_{\perp,\parallel}$) and also a weak photo-induced response from the SiC substrate $\Delta\sigma_{\text{SiC}}$; ϕ stands for the absorbed fluence of the pump pulse. The sheet conductivities in the excited and ground state are described by the Lorentz model for perpendicular configuration and by the modified Drude-Smith response for parallel configuration: [18]

$$\sigma_{\perp}(\omega) = \frac{wD}{L\pi} \frac{i\omega}{\omega^2 - \omega_0^2 + \frac{i\omega}{\tau_{s,\perp}}} \quad (4)$$

$$\sigma_{\parallel}(\omega) = \frac{wD}{L\pi} \frac{\tau_{s,\parallel}}{1 - i\omega\tau_{s,\parallel}} \left(1 + \frac{c}{1 - \frac{i\omega d^2}{5v_F^2\tau_{s,\parallel}}} \right) \quad (5)$$

where $w/L = 87\%$ is the filling fraction of the graphene component, c describes the degree of localization of charge carriers and d is the characteristic dimension of the carrier confinement. The response is controlled by the Drude weight D and the geometry of nanoribbons, both determining the plasmonic resonance frequency ω_0 :

$$D = \frac{2e^2}{\hbar^2} k_B T_c \ln \left[2 \cosh \left(\frac{\mu(T_c)}{2k_B T_c} \right) \right], \quad (6)$$

$$\omega_0 = \sqrt{\frac{D(T_c)w}{\varepsilon_0(1 + \varepsilon_{\text{SiC}})L^2 \ln\left(\sec\left(\frac{\pi W}{2L}\right)\right)}}. \quad (7)$$

In the ground state, the carrier temperature T_c is equal to 300 K. In the excited state, the carrier temperature is generally elevated. Furthermore, with an increasing pump fluence, the carrier density can be significantly modified alongside with the carrier temperature and momentum scattering time. This results in a small correction in the Fermi energy due to excess carriers resulting from the optical excitation.

$$E_F(\tau_p) = \sqrt{E_{F,SS}^2 + q(\tau_p)\phi\pi\hbar^2v_F^2}, \quad (8)$$

where $E_{F,SS}$ is the steady-state (SS) Fermi energy and q is a proportionality factor between 0 and 1 providing the fraction of non-recombined photocarriers at the time delay τ_p . The chemical potential can be evaluated from the energy conservation law [20]

$$\frac{1}{2}\left(\frac{E_F}{k_B T_c}\right)^2 = F_1\left(\frac{\mu}{k_B T_c}\right) - F_1\left(-\frac{\mu}{k_B T_c}\right), \quad (9)$$

where F_1 is the first order Fermi-Dirac integral. Unfortunately, Eq. (9) yields a strong correlation between the photoexcited carrier density (determined by q) and temperature (T_c). Since our measurements were performed 2 ps after photoexcitation, we neglect in the first approximation the recombination during this short period, and we fix the photo-carrier fraction to $q = 1$. The global fitting of the transient spectra in the perpendicular orientation, Fig. 3(b), provides the carrier scattering time and temperature as a function of the pump fluence and the steady-state Fermi energy value $E_{F,SS} = 310$ meV (global parameter). The spectra in the parallel orientation, Fig. 3(a), are fitted using the carrier temperature values obtained from the fits in the perpendicular geometry leaving just the carrier scattering time and the confinement parameter c as free parameters (independently fit for each fluence), along with the confinement length $d \approx 250$ nm (global parameter for all spectra). Further details on the fitting procedure and possible interpretations of the confinement length were discussed in [18]. The evolutions of all the directly fitted parameters (scattering times, carrier temperature and confinement parameter) are shown in Fig. 4(a–c). The chemical potential, Drude weight, carrier mobility and plasmon resonance frequency are calculated from these fitted values and they are shown in Fig. 4(d–g).

Let us mention that the determined steady-state value of the Fermi energy corresponds to the free carrier concentration of $\sim 7 \times 10^{12} \text{ cm}^{-2}$. After photoexcitation, these carriers (or

their part) will form the secondary (hot) carriers. The behavior of the investigated system can be divided into several distinct regimes. For the low fluence regime ($\phi \lesssim 1 \times 10^{12}$ photons cm^{-2}), the carrier temperature almost linearly increases with the fluence since the secondary hot carrier generation is efficient and, consequently, the chemical potential and the Drude weight decrease rapidly [Fig. 4(d,e)]. As a consequence, and despite of a small decrease in the scattering time (Fig. 3), a small increase in the mobility $\eta = \tau_s e_0 v_F^2 / \mu(T_c)$ is observed with an increasing pump fluence. The plasmon frequency exhibits a red shift.

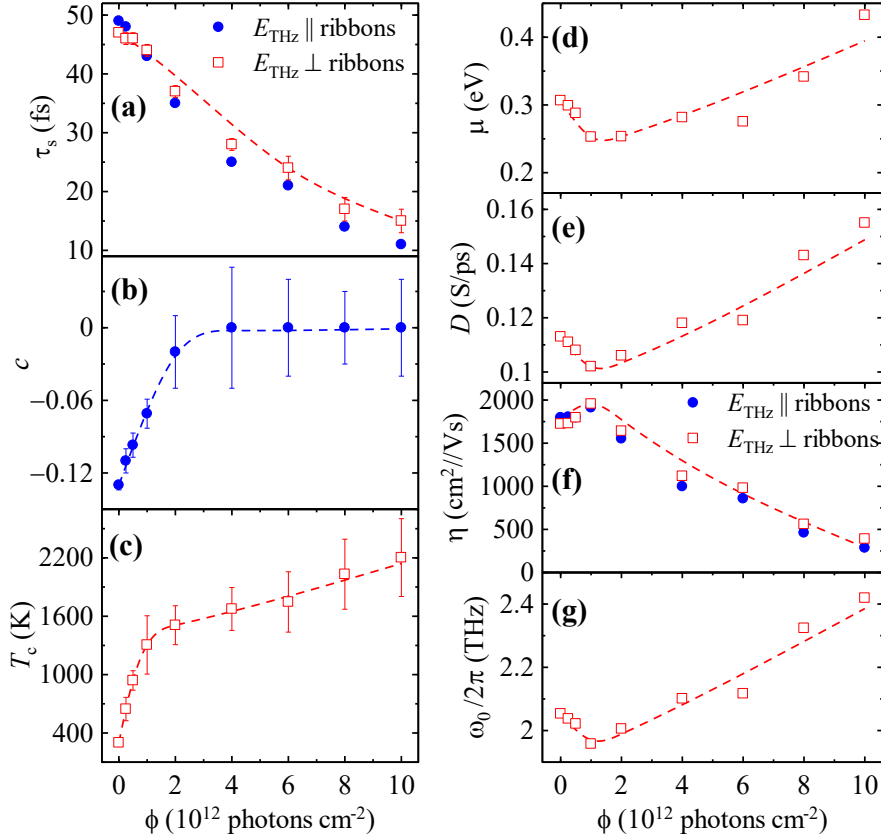


Figure 4: Evolution of the directly fitted parameters with the absorbed pump fluence: (a) scattering times τ_s , (b) localization parameter c , and (c) carrier temperature T_c . Evolution of the calculated transport parameters and plasmonic frequency from the fit parameters: (d) chemical potential μ , (e) Drude weight D , (f) mobility η , and (g) plasmonic frequency ω_0 . Red symbols are obtained from the spectra for $E_{\text{THz}} \perp$ ribbons and blue symbols are obtained from the spectra for $E_{\text{THz}} \parallel$ ribbons. Dashed lines are guides for the eyes.

Conversely, in the high fluence regime ($\phi \gtrsim 4 \times 10^{12}$ photons cm^{-2}), the generation of secondary hot carriers is much less efficient, since there is a limited number of equilibrium conduction carriers. As a result, the contribution of newly excited (excess) carriers takes over and this leads to an increase in the Drude weight, which compensates the observed decrease in the scattering time in Fig. 4(a). This balance accounts for the observed saturation of the photoconductivity amplitude [Fig. 2(b), top panel]. In this regime the decay time extends and

its growth does not saturate at the highest fluences [Fig. 2(b), bottom panel]; this is because all the conduction carriers are hot and, e.g., the Auger recombination process is inhibited. In this regime, the decrease in the carrier scattering time is not compensated by the drop of the chemical potential, thus leading to a decrease of the carrier mobility up to a factor of 4 (still under the assumption that all photocarriers remain in the conduction band till 2 ps after photoexcitation). The observed variation of the Drude weight leads to a complex behavior of the plasmon resonance; indeed, the red shift observed at low fluences is followed by a significant blueshift at high fluences due to the presence of excess carriers.

The significant decrease of the scattering time excludes the state filling effects of pump photons in the conduction band. A weak localization of carriers ($c < 0$) was previously reported in this sample [18]; now it becomes clear that the localization is progressively lifted and it completely disappears ($c \rightarrow 0$) for $\phi \gtrsim 4 \times 10^{12}$ photons cm^{-2} , see Fig. 4(b). This confirms that the localization is controlled by energy barriers that are overcome by the hot carriers owing to their increased kinetic energy at elevated carrier temperatures.

4. Conclusion

We observed that increasing the fluence of optical excitation pulses drives the graphene into three distinct regimes. (i) ($\phi \lesssim 10^{12}$ photons/ cm^2) Weakly confined charges, increase of temperature and decrease of chemical potential, (ii) transition (intermediate) regime exhibiting a minimum of the chemical potential and a maximum of the mobility due to an interplay of excess carriers and the equilibrium conduction carriers heated by the pump-deposited energy, and (iii) high fluence regime ($\phi \gtrsim 4 \times 10^{12}$ photons/ cm^2), where the excess carriers dominate and which is characterized by a saturation of the carrier temperature and conductivity.

Acknowledgment

We acknowledge the financial support by Czech Science Foundation (grant number 24-10331S) and by European Union and the Czech Ministry of Education, Youth and Sports (Project TERA FIT - CZ.02.01.01/00/22_008/0004594). Finally, CzechNanoLab project LM2023051 funded by MEYS CR is acknowledged for the financial support of the sample fabrication at CEITEC Nano Research Infrastructure.

References

- [1] K. J. Tielrooij, J. C. W. Song, S. A. Jensen, A. Centeno, A. Pesquera, A. Zurutuza Elorza, M. Bonn, L. S. Levitov, and F. H. L. Koppens, *Photoexcitation Cascade and Multiple Hot-Carrier Generation in Graphene*, *Nature Phys* **9**, 4 (2013).
- [2] Z. Mics, K.-J. Tielrooij, K. Parvez, S. A. Jensen, I. Ivanov, X. Feng, K. Müllen, M. Bonn, and D. Turchinovich, *Thermodynamic Picture of Ultrafast Charge Transport in Graphene*, *Nat Commun* **6**, 7655 (2015).
- [3] M. T. Mihnev et al., *Microscopic Origins of the Terahertz Carrier Relaxation and Cooling Dynamics in Graphene*, *Nat Commun* **7**, 11617 (2016).
- [4] N. M. Gabor, J. C. W. Song, Q. Ma, N. L. Nair, T. Taychatanapat, K. Watanabe, T. Taniguchi, L. S. Levitov, and P. Jarillo-Herrero, *Hot Carrier-Assisted Intrinsic Photoresponse in Graphene*, *Science* **334**, 648 (2011).
- [5] D. Sun, G. Aivazian, A. M. Jones, J. S. Ross, W. Yao, D. Cobden, and X. Xu, *Ultrafast Hot-Carrier-Dominated Photocurrent in Graphene*, *Nature Nanotech* **7**, 114 (2012).
- [6] M. Massicotte, G. Soavi, A. Principi, and K.-J. Tielrooij, *Hot Carriers in Graphene – Fundamentals and Applications*, *Nanoscale* **13**, 8376 (2021).
- [7] A. Singh and S. Kumar, *Phonon Bottleneck in Temperature-Dependent Hot Carrier Relaxation in Graphene Oxide*, *J. Phys. Chem. C* **125**, 26583 (2021).
- [8] A. Singh and S. Kumar, *Terahertz Photonics and Optoelectronics of Carbon-Based Nanosystems*, *Journal of Applied Physics* **131**, 160901 (2022).
- [9] E. A. A. Pogna et al., *Hot-Carrier Cooling in High-Quality Graphene Is Intrinsically Limited by Optical Phonons*, *ACS Nano* **15**, 11285 (2021).
- [10] P. Kužel and H. Němec, *Terahertz Spectroscopy of Nanomaterials: A Close Look at Charge-Carrier Transport*, *Advanced Optical Materials* **8**, 1900623 (2020).
- [11] V. C. Paingad, J. Kunc, M. Rejhon, I. Rychetský, I. Mohelský, M. Orlita, and P. Kužel, *Ultrafast Plasmon Thermalization in Epitaxial Graphene Probed by Time-Resolved THz Spectroscopy*, *Advanced Functional Materials* **31**, 2105763 (2021).
- [12] J.-C. Deinert et al., *Grating-Graphene Metamaterial as a Platform for Terahertz Nonlinear Photonics*, *ACS Nano* **15**, 1145 (2021).
- [13] H. A. Hafez et al., *Extremely Efficient Terahertz High-Harmonic Generation in Graphene by Hot Dirac Fermions*, *Nature* **561**, 507 (2018).
- [14] H. A. Hafez, S. Kovalev, K.-J. Tielrooij, M. Bonn, M. Gensch, and D. Turchinovich, *Terahertz Nonlinear Optics of Graphene: From Saturable Absorption to High-Harmonics Generation*, *Advanced Optical Materials* **8**, 1900771 (2020).
- [15] J. W. Han et al., *Plasmonic Terahertz Nonlinearity in Graphene Disks*, *Advanced Photonics Research* **3**, 2100218 (2022).
- [16] J. Kunc, M. Rejhon, E. Belas, V. Dědič, P. Moravec, and J. Franc, *Effect of Residual Gas Composition on Epitaxial Growth of Graphene on SiC*, *Phys. Rev. Appl.* **8**, 044011 (2017).
- [17] J. Kunc, M. Rejhon, and P. Hlídek, *Hydrogen Intercalation of Epitaxial Graphene and Buffer Layer Probed by Mid-Infrared Absorption and Raman Spectroscopy*, *AIP Advances* **8**, 045015 (2018).
- [18] A. Singh, H. Němec, J. Kunc, and P. Kužel, *Nanoscale Terahertz Conductivity and Ultrafast Dynamics of Terahertz Plasmons in Periodic Arrays of Epitaxial Graphene Nanoribbons*, *Phys. Rev. Res.* (2024), in press.
- [19] H.-K. Nienhuys and V. Sundström, *Intrinsic Complications in the Analysis of Optical-Pump, Terahertz Probe Experiments*, *Phys. Rev. B* **71**, 235110 (2005).
- [20] E. H. Hwang and S. Das Sarma, *Screening-Induced Temperature-Dependent Transport in Two-Dimensional Graphene*, *Phys. Rev. B* **79**, 165404 (2009).